Forced Rotational Motion of Fluid in a Cavity: A Molecular Dynamics Study

Eric C. J. Oliver*

Department of Oceanography,

Dalhousie University,

1355 Oxford St., Halifax,

NS, Canada, B3H 4J1

Gary W. Slater†

Department of Physics,

University of Ottawa,

150 Louis-Pasteur, Ottawa,

ON, Canada, K1N 6N5

(Dated: June 13, 2007)

Abstract

We have performed Molecular Dynamics simulations of microscale laminar flow in a coupled channel-cavity system in order to explore forced rotation of the fluid in the cavity by the channel flow. These simulations have reproduced experimental observations well. We have extended our treatment to explore how modifying the surface tension along the walls of the channel affects the slip length. By applying this to the coupled channel-cavity system we can affect the efficiency of spin generation in the cavity fluid. For a constant flow rate, we find that we can generate a 70-80% higher spin rate in the cavity by decreasing the surface tension of the walls (using two possible schemes) by about 50%.

I. INTRODUCTION

The miniaturization of fluidic systems to the micro- and nano-scale is proving its usefulness across the laboratory spectrum and there is much research on the physics of fluids occuring on these small scales[1]. Recent developments are progressing towards the point where all operations on microfluidic systems will be done "on-a-chip" and laboratories will use micro-devices that can perform operations such as chemical reactions, mixing, molecular separations and other basic functions.

An example of one such function we consider is the centrifugation of a small volume of fluid. An experimental situation has already been devised by Shelby *et al.*[2] where a small fluid-filled cavity approximately 50 μm across has been forced into rotation by coupling it to pressure-driven flow in a channel of similar cross-sectional dimensions and a length of 150 μm. With average fluid velocities of up to 45 m/s in the channel, rotational velocities as high as 12 m/s at a distance of 12 μm from the core of the resulting vortex were observed. This corresponds to a radial acceleration of 1.4×10^6 g. It was also observed that the rate of fluid rotation in the cavity increases with the flow rate in the channel. In later experiments, this group has demonstrated a practical use for a device operating on this principle by placing a biological cell in the cavity and using the rotational flow to examine the effects of stress on the cell[3,4]. Other uses for such a device that will be practical in microfluidic systems are also apparent. Such applications could include the centrifugation and separation of a multi-component fluid mixture as well as the possibilities of mixing or dilution of a solution using rotating cavity fluid and possible mass exchange between the cavity and the channel.

In this paper, we simulate this experimental system using a two-dimensional Molecular Dynamics computational algorithm. The basic physics that were observed experimentally are reproduced in our simulations. In addition, we explore avenues to enhance the efficiency of spin generation in the cavity fluid by changing the attractive interactions between the solid wall and the fluid. This change results in a modified surface tension. To maximize the radial acceleration in the microcavity, surface tension was reduced and thus the fluid slips along the wall near the coupling region with the cavity. We also employed predictions from macroscopic hydrodynamics in situations where experimental results give no indication of what is expected.

Two-dimensional Molecular Dynamics simulations such as the one employed here have

been used in the past to succesfully model various fluidic systems. Notably, there have been studies of the evolution of flow patterns around solid obstacles[5,6], Rayleigh-Bernard convection[7,8] and reproduction of the laminar flow characteristics of a Navier-Stokes fluid[9]. All have used two-dimensional simulations and the results agree well with what is expected from three-dimensional models. From the studies of flow around obstacles, the simulation field represents a cross section through a three-dimensional system where the geometry is independent of the direction perpendicular to the cross section. Furthermore, there have been studies which examine more explicitly the behaviour of two-dimensional Molecular Dynamics models of fluids with regards to their accuracy and representaion of three-dimensional predictions[10,11]. These studies, along with the computational efficiency gained over three-dimensional simulations, demonstrate the usefulness of two-dimensional simulations as reasonable models of certain three-dimensional systems. It should be noted that the parameters used in the simulations presented here are such that the temperature and density of the fluid lie above their respective critical points[12]. The parameters were chosen in order to avoid liquid layering across the channel and to ensure that the fluid was incompresible enough that we can apply strong pressure gradient forces. Therefore, the results shown here do not correspond to a specific fluid but must be interpreted as representative of a generic fluid.

This paper is organized into four sections. First, we will present the fluidic system along with the relavent hydrodynamic theory. Then, we will review our Molecular Dynamics simulation method and how we apply it to our system. The last two sections deal with the simulation results. In the third section, we discuss the channel alone, such as its hydrodynamic properties and measurements of slip length. Finally, we present the cavity results, including measurements of its spin and how we can increase the efficiency of spin generation.

II. SYSTEM

The system we are modelling is a simplified and idealized version of the experimental setup used by Shelby *et al.*[2–4] and consists of a narrow channel with flow driven by a pressure gradient which is coupled to a small circular cavity situated along one of the channel walls (see Fig. 1 for details). Viscous coupling is achieved through a small opening in the upper wall which allows contact and thus transfer of momentum between the fluid in the channel and the cavity. The problem essentially consists of the classic lid-driven cavity[13,14] but with

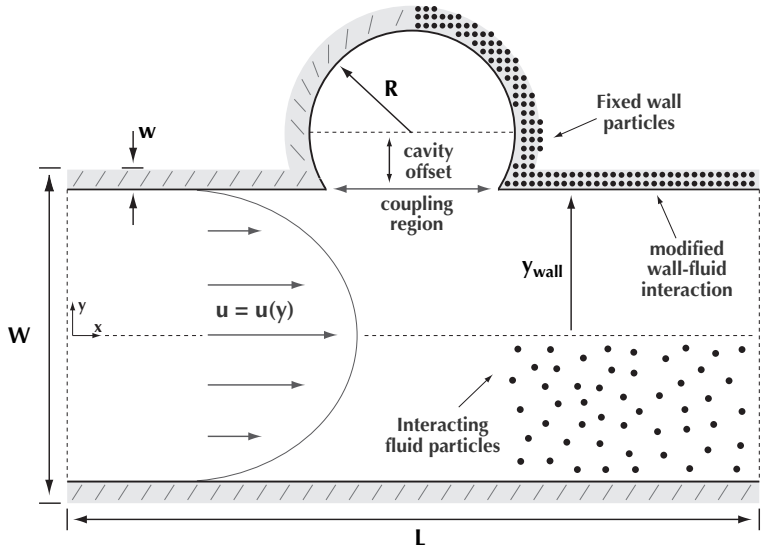

FIG. 1: Schematic of the coupled channel-cavity system. The channel is $W = 55.9\,\sigma$ in width (including the walls of thickness $w = 2.23\,\sigma$) and $L = 134.16\,\sigma$ in length. The circular cavity has a radius $R = 12.3\,\sigma$ and is offset from the position of the channel wall by $11.18\,\sigma$. A Poiseuille flow is generated in the channel which is coupled to the cavity and drives rotational motion of the fluid in the cavity. Also presented here are representations of the wall and fluid in terms of interacting particles which are used in the Molecular Dynamics simulations.

the driving lid replaced by coupling the cavity to the fluid flow in the channel. The width of the opening which serves as the coupling region is chosen to be on the order of the radius of the cavity so that there can be substantial channel-cavity coupling but not reduce the cavity to a mere indentation along the wall. If the channel flow is nonzero along the upper wall, then the fluid in the cavity will be dragged along its outer edge and driven into rotational motion. A simple property of the system is that the tangential velocity, $u_{\rm t}$, in the cavity, and thus the radial acceleration, $a_{\rm r}$, is limited by the fluid flow in the coupling region: $u_{\rm t} \leq u_{\rm wall}$, where $u_{\rm wall}$ is the fluid velocity at the wall. With a circular vortex generated in the cavity of radius R this implies a maximum radial acceleration $a_{\rm r} \leq u_{\rm wall}^2/R$.

We will model the system in two dimensions for the following reasons: efficient computation and simplicity without loss of essential physics for comparing the results to experiments and three-dimensional simulations. Essentially, we are implying that our results should hold for systems which are very large in the z-direction (perpendicular to the figure) such that

we are observing the physics of a single slice parallel to the xy-plane. The physics within each slice will be very similar if not identical and thus by modelling in only two dimensions we can recover the dynamics within one of these slices.

As is well known, flow is laminar in systems with low Reynolds numbers (for $\mathrm{Re} \lesssim 10^3$). If the fluid is confined by two plates parallel to the xz-plane positioned at $\pm y_0$ and is driven by an external acceleration g in the x-direction then the resulting Poiseuille flow assumes the following quadratic profile[15]:

$$u(y) = \frac{\rho_0 g}{2\eta} \left(y_0^2 - y^2 \right), \tag{1}$$

where η is the shear viscosity (or dynamic viscosity, sometimes denoted by μ) of the fluid and ρ_0 is the average density of fluid. In this study, the Reynolds number is typically $\sim$O(10) and so the flow lies in the laminar regime (but not so low that it is in the Stokes flow regime, *i.e.* $\mathrm{Re} \ll 1$). Note that more commonly, Poiseuille flow is generated by applying a pressure gradient dp/dx. In this case, the form of the flow profile will be the same as Eq. 1 except with the substitution of $\rho_0 g = -dp/dx$.

The Poiseuille velocity profile is such that the velocity vanishes at the walls. This is called the *no-slip* boundary condition, a common assumption used in continuum fluid dynamics. In reality, depending on the wall-fluid interaction and the external force or pressure difference, there can be a small amount of slip at the wall. We can characterize the extent of the slip using the *slip length*, δ, which is the distance from the wall where the velocity profile is extrapolated to zero.

III. SIMULATION METHOD

In order to simulate the system described in Section II, we use Molecular Dynamics (MD) computer simulations which allow us to resolve the processes that occur on the molecular scale; in this regime the precepts of macroscopic fluid dynamics may no longer hold since we are no longer dealing with bulk fluid. It has been shown that the predictions of continuum hydrodynamics are recovered from MD within a few particle layers[16], a claim upheld by the smooth Poiseuille-like flow we generate. However, due to the inherently coarse-grained nature of the MD model, we are studying a generic fluid and cannot make claims to the exact system dimensions and parameter values. As will be seen, we observe the structure of

the fluid to be based on finite particles and so we are very close to the nanoscale; however, a large portion of the system exists in bulk conditions and reproduces the predictions of macroscopic hydrodynamics and so our results should hold for microscale systems in which bulk fluid properties are observed.

We model the fluid and wall constituents by using beads (see Fig. 1 for an example) which interact through the cut-and-shifted Lennard-Jones (LJ) pair potential:

$$U_{ij} = \begin{cases} 4\epsilon \left[\left(\frac{\sigma}{r_{ij}}\right)^{12} - c_{ij} \left(\frac{\sigma}{r_{ij}}\right)^{6} \right] + \epsilon_0 & \text{if } r_{ij} \leq r_{\mathrm{c}} \\ 0 & \text{if } r_{ij} > r_{\mathrm{c}}, \end{cases} \tag{2}$$

between any two particles i and j, where σ and ϵ are constants which set the length and energy scales, respectively. For computational efficiency we have cut off the LJ potential for $r_{ij} > r_{\mathrm{c}} = 2.5\,\sigma$ and shifted the potential up by a small amount $\epsilon_0 \equiv -U(r_{\mathrm{c}})$ to ensure that U is continuous. This is a common choice and retains both the repulsive core and most of the attractive tail of the potential[17]. All parameters herein are quoted in natural MD units: $m = \epsilon = \sigma = 1$ (m is the particle mass) and the unit of time is $\tau = \sqrt{m\sigma^2/\epsilon}$. Note that it is possible to simulate real materials using this method. For example, Argon would have the parameter values $\sigma = 0.34$ nm, $\epsilon = 1.654 \times 10^{-21}$ J and $m = 6.6904 \times 10^{-26}$ kg[17]. The particles are initialized on a square lattice with an average density (for both the fluid and the wall) of $\rho_0 = 0.8/\sigma^2$. The temperature is set by initializing the fluid particle velocities according to the Maxwell distribution about a mean of $k_{\mathrm{B}}T = 1\,\epsilon$ and it is kept constant through the use of a thermostat based on the principles of dissipative particle dynamics (DPD)[18]. Care was taken to avoid known timestep issues with this thermostat[19]. The factor c_{ij} in Eq. 2 is a constant, of order one, which controls the strength of the attractive tail of the LJ potential, and we will use it to tune the strength of the wall-fluid interactions. The Newtonian equations of motion for the particles are integrated using the velocity-Verlet algorithm with a timestep of $\Delta\tau = 0.01\,\tau$ and the computations are made more efficient by using linked cells and neighbour lists[17]. The wall particles are kept fixed in position. In many other models the wall particles are kept in a deep potential well and allowed to exchange momentum and energy with the fluid particles. While our choice is less realistic, we are confident it has no effect on the object of this study other than having the thermostat exercising larger influence since the wall particles are unable to cool the fluid by extracting energy. The walls confine the fluid in the y-direction and we impose periodic boundary

conditions in the x-direction.

Two types of channels are considered: one with only fluid and channel walls and another with a cavity placed along one of the walls. The size of the channel-only system is $L = 111.8\,\sigma$ by $W = 55.9\,\sigma$ (with two layers of wall particles taking a width $w = 2.23\,\sigma$ of that on each side). This system is used to measure the effect of both the wall-fluid interaction strength and the fluid flow rate on slip length. The size of the system with the cavity extends to $L = 134.16\,\sigma$ long with the 'spin-cavity' placed halfway along down the channel at the upper wall. It is circular with a radius of $R = 12.3\,\sigma$ and its centre is offset by $11.18\,\sigma$ from the fluid-wall interface (see Fig. 1). This allows the cavity to have a localised section of its perimeter open to the flow in the channel. In order to simulate a Poiseuille flow which is created experimentally by a pressure drop along the channel we applied a constant acceleration to all particles in the channel (but not to the particles in the cavity). As will be demonstrated, this creates a flow profile that varies quadratically across the channel as expected according to Eq. 1.

Technically speaking our simulations consist of $N = 5000$ particles for simulations in Section IV (consisting of 4600 fluid particles and 400 wall particles) and $N = 8400$ particles for simulations in Section V (consisting of 5898 fluid particles and 2502 wall particles). The MD algorithm is executed on two 3.4 GHz Intel Pentium 4 CPU with 1 and 2 GB of RAM each. Each simulation is run for 7.5×10^6 timesteps and takes one to three days to complete.

IV. RESULTS I: THE CHANNEL PROPERTIES

A. Wall Position

In order to analyse the slip length and measure the velocity at the wall, it is necessary to determine the effective position of the wall surface. Since we have a molecularly rough wall this is not a trivial task. A simple measure is to say that the wall begins at the centre of the first particle of the wall but this is not a robust measure of the wall position as there will be a finite region around the centre of the wall particles where no fluid particles will penetrate due to the strong repulsive interaction. This property is clearly observable from the particle distribution function near the wall (see Fig. 2). Instead we opt for an unambiguous measure based on a simple geometric argument[20]. The area the fluid occupies can be computed as

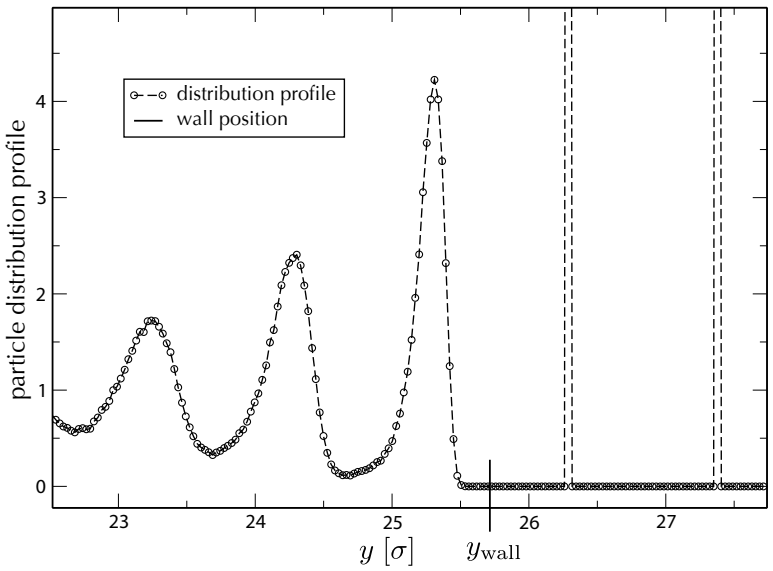

FIG. 2: Particle distribution profile across the channel. Note the presence of the two fixed layers of wall particles at $y = 26.27\,\sigma$ and $y = 27.39\,\sigma$ as well as the layering of the fluid induced by the rigid wall (layers shown peak at $y = 23.24\,\sigma$, $y = 24.30\,\sigma$ and $y = 25.31\,\sigma$). The distribution profile is normalized such that it goes to 1 in the central region of the channel (about $y = 0$, see Fig. 3). The geometric position of the wall, denoted by $y_{\rm wall}$, is shown in the figure at $y = 25.71\,\sigma$.

the number of fluid particles N divided by the mean density, ρ_0. The area is also equal to the total length of the system (since it is periodic along x), L, times the width of the channel, which can be expressed as twice the distance to the wall $2y_{\rm wall}$, and so we have the relation $2Ly_{\rm wall} = N/\rho_0$, from which we can find the wall position:

$$y_{\rm wall} = \frac{N}{2L\rho_0}. \tag{3}$$

Using $N = 4600$, $L = 111.8\,\sigma$ and $\rho_0 = 0.8/\sigma^2$ we find the result: $y_{\rm wall} = 25.71\,\sigma$ (which is noted on the particle distribution profile in Fig. 2).

B. Hydrodynamic Properties

We can use the wall position to predict some of the hydrodynamic properties of the fluid. For a basic channel with straight walls and an external acceleration of $g = 0.025\,\sigma/\tau^2$ we recover a nearly quadratic flow profile (see Section IV D for further discussion on this). Using Eq. 1 with the parameters $\rho_0 = 0.8/\sigma^2$ and $y_0 = y_{\rm wall} = 25.71\,\sigma$, we can perform a fit to the

flow profile data and recover the shear viscosity $\eta = 7.08 \pm 0.02\ \sqrt{m\epsilon}/\sigma$. Furthermore, the Reynolds number is defined as

$$\mathrm{Re} = \frac{\rho_0 \bar{u} d}{\eta} \tag{4}$$

where $\bar{u}$ is the fluid velocity averaged over the cross section of width d. Using $d = 2y_{\mathrm{wall}}$ and $\bar{u} \simeq 1\ \sigma/\tau$ (which is appropriate for what we observe) we can calculate the Reynolds number for our flow to be $\mathrm{Re} \simeq 6 \ll 10^3$. This demonstrates that our MD fluid flow simulations are certainly in the laminar flow regime.

C. Fluid-wall Surface Tension

In order to vary the interaction between the fluid and the wall particles, and consequently the slip length, it is important to have a physical representation for this variation. Essentially, what characterises the fluid-wall interface is the effective interaction energy U_{fw} between the wall and the fluid. From Laplace's formulation for surface tension[21] we can use this to calculate the surface energy density or surface tension. The surface tension, γ_{fw}, can be expressed as[22]

$$\gamma_{\mathrm{fw}} = -\frac{1}{8}\rho_{\mathrm{w}}\rho_{\mathrm{f}} \int_d^\infty r U_{\mathrm{fw}}(\boldsymbol{r}) d\boldsymbol{r} \tag{5}$$

where $U_{\mathrm{fw}}(r)$ is the Lennard-Jones interaction energy between the fluid and wall particles, ρ_{w} and ρ_{f} are the wall and fluid densities, respectively, and d is the point at which $U_{\mathrm{fw}}(r) = 0$. In two dimensions we have $d\boldsymbol{r} = r d\theta dr$ where we integrate θ over a full circle. From Eq. 2 we can calculate $d = \sigma/c_{\mathrm{fw}}^{1/6}$, and by substituting this and the interaction energy into Eq. 5, we can derive the surface tension of our interface:

$$\gamma_{\mathrm{fw}} = \frac{2\pi}{9}\rho_{\mathrm{w}}\rho_{\mathrm{f}}\epsilon\sigma^3 c_{\mathrm{fw}}^{3/2}. \tag{6}$$

Thus, the surface tension is expected to increase monotonically and nonlinearly with the strength of attractive interaction, c_{fw}. It should be noted that since we are working in 2D, this is not technically a "surface" tension but actually a "line" tension with units of energy per unit length.

The interaction energy (and thus surface tension) between the wall and fluid can also be controlled by changing the energy scale ϵ_{fw}. Previous studies exploring fluid slip and wetting phenomena dependence on the interaction potential have been done using both the constant c_{fw}[22–24] as well as the energy scale[25–27]. Either choice will have a similar effect on the

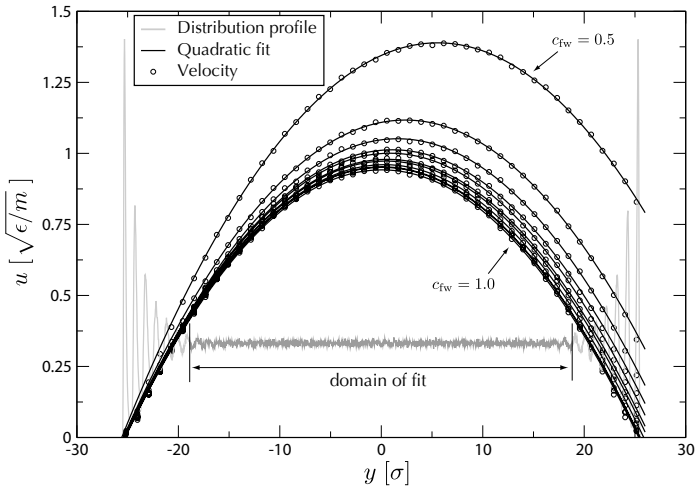

FIG. 3: Equilibrium velocity profiles for various levels of interaction between the fluid and the wall particles (with $g = 0.025\,\sigma/\tau^2$). The velocity was calculated by averaging the steady-state particle velocities in 50 bins across the channel. $c_{\rm fw}$ is on the upper wall is varied from 0.5 to 1.0 in increments of 0.05. Included in the figure is the particle distribution profile (arbitrary units) for the $c_{\rm fw} = 1.0$ case. The domain of the fit is limited to where this density profile is approximately constant and the fluid resembles bulk conditions. For these simulations the system size is $L = 111.8\,\sigma$ and $W = 55.9\,\sigma$ and there is no cavity (just straight walls at $\pm y_{\rm wall}$.)

surface tension: increasing the magnitude of the interaction will increase the surface tension. The studies referenced above have shown that $c_{\rm fw} < 1$ represent hydrophobic conditions. Consequently, we will only modify this parameter and set $\epsilon = 1$ for all interactions.

D. Slip Length

As described in Section II, the maximum radial acceleration inside the cavity is limited by the fluid velocity at the channel-cavity interface. If the applied acceleration, g, of the fluid is increased we would expect the velocity at the wall to increase accordingly. Thus, as is observed experimentally, the rate at which cavity fluid rotates should increase with flow rate[2,4] and thus g (according to Eq. 1). However, rather than use g to achieve larger radial accelerations in the cavity, we are proposing that one can simply modify the surface tension at the wall and achieve a larger fluid velocity than for an unmodified wall at the same acceleration (or flow rate).

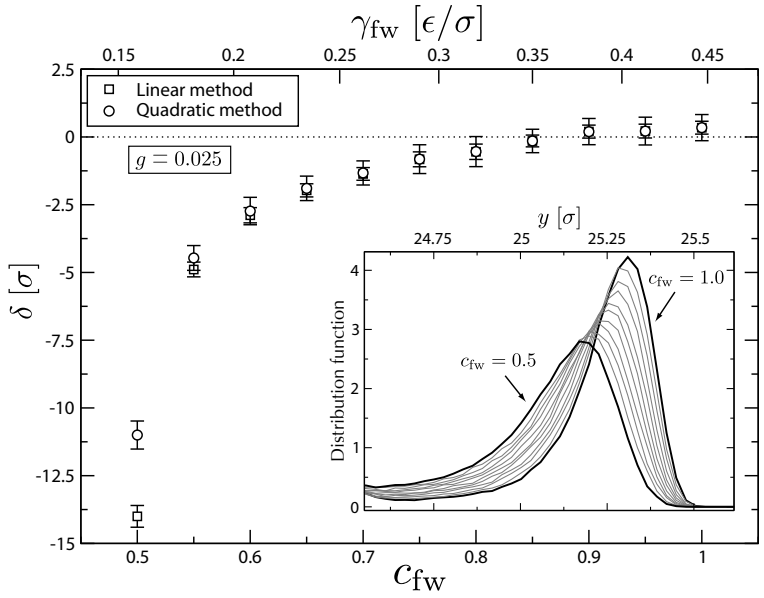

FIG. 4: Slip length δ at upper wall as a function of fluid-wall interaction for both the linear extrapolation and the quadratic fit methods. The magnitude of slip length increases with decreasing $c_{\rm fw}$ (interaction strength) or $\gamma_{\rm fw}$ (surface tension). The inset shows the distribution profile for particles near the wall. The rightmost curve corresponds to $c_{\rm fw} = 1.0$ and each neighbouring curve decreases by $\Delta c_{\rm fw} = 0.05$ until the last curve at $c_{\rm fw} = 0.5$ (always with a constant $g = 0.025\ \sigma/\tau^2$). As $c_{\rm fw}$ is decreased the position of the peak of the distribution moves further from the wall. Interestingly, we note that for the smallest surface tensions, the slip length is on the order of the size of the cavity which will be placed along that wall (i.e., $\delta \sim R$).

In order to vary the slip length and thus the velocity at the wall, we tune the c_{ij} parameter in Eq. 2 for fluid-wall interactions. Reference simulations were performed in a test channel with no cavity (as described in Section III). The lower wall always has fluid-wall interactions with $c_{\rm fw} = 1$ (the pure LJ, or wetting[24], case) while the upper wall is varied in separate simulations from $c_{\rm fw} = 0.5$ to $c_{\rm fw} = 1$ in steps of size $\Delta c_{\rm fw} = 0.05$. The resulting velocity profiles, taken as an average after the system has reached a steady state velocity, is shown in Fig. 3. For $c_{\rm fw} = 1$ we recover a quadratic Poiseuille flow profile which vanishes in the vicinity of the wall. As expected, we see that decreasing the value of $c_{\rm fw}$ on the upper wall increases the velocity of the fluid near the wall and thus the slip length. Similar phenomena have been observed by Koplik *et al.*[23]. Furthermore, and as a comparison, we have performed simulations with $c_{\rm fw} = 1$ at both walls and varied g in order to see the slip produced by

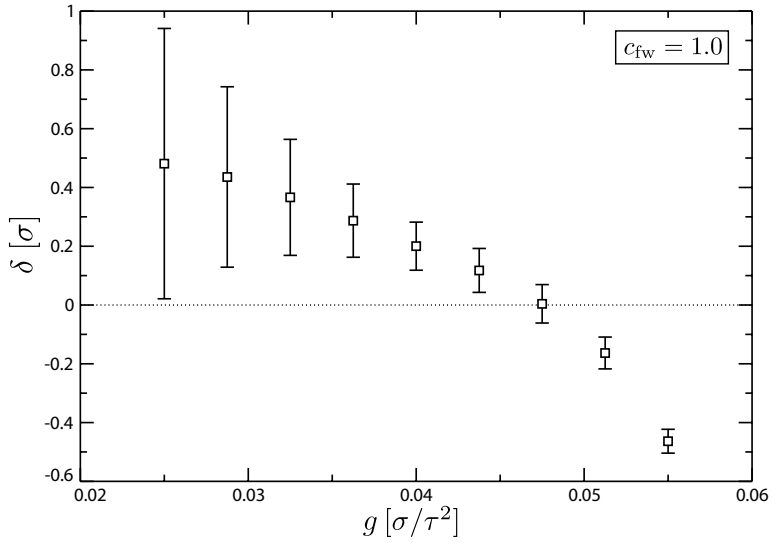

FIG. 5: Slip length δ as a function of applied acceleration g using the linear extrapolation method. The parameter c_{fw} is always constant at a value of 1.0. The quadratic method yields nearly identical values so we have left them off this figure for simplicity. As expected, the slip length becomes more negative as g increases. When $g \to 0$ the slip length corresponds to the position of the first layer of fluid near the wall.

increasing the acceleration.

The speed of the fluid at the upper wall, $u_{\mathrm{wall}} \equiv u(y_{\mathrm{wall}})$, which will be related to the slip length, is likely to be a significant factor in driving the rotation of the fluid in the cavity. We will refer to this value as the slip velocity. If it is nonzero, there is slip; if it is zero, there is no slip. Thus, we explore how the slip length depends on the fluid-wall interaction. The slip length, δ, for Poiseuille flow can be determined in two ways: by linear extrapolation or by quadratic fitting. The first method involves extrapolating the velocity linearly using a slope taken from the flow profile at the wall and determining at what value of y the velocity would go to zero. This can be expressed as a boundary condition:

$$\left.\frac{du}{dy}\right|_{y_{\mathrm{wall}}} = \frac{u_{\mathrm{wall}}}{\delta}. \tag{7}$$

The second method involves fitting the velocity profile data set with a quadratic function and then finding the point at which the function vanishes. In both cases the slip length is defined as the difference between the position of the wall, y_{wall}, and the position at which the extrapolated velocity goes to zero, y_0: $\delta = y_{\mathrm{wall}} - y_0$. The former method benefits from

simplicity whereas the latter is more consistent with quadratic nature of pressure-driven flow profiles. Clearly, both methods will yield a different result, and in that sense the quantitative value of the slip length becomes simply a matter of definition.

To measure the slip length we fit the velocity profile using one of the above methods, for each value of c_{fw} and g. We expect the velocity profile to be fit well by a quadratic in accordance with macroscopic Poiseuille flow, with the exception that the velocity does not go to zero at the walls. Also, near the wall the fluid particles exist in layers and thus in that region we cannot expect the macroscopic prediction of hydrodynamics to hold (since the predictions were all derived assuming constant density, viscosity, etc.). Therefore, the quadratic fit to the data is restricted to the subset of points that lie within the region of the channel where the particle distribution is approximately constant rather than across the whole channel which would include the layered fluid seen near the wall (see Fig. 3). For the simulations where g is varied, the data is fit with a fourth order polynomial (ignoring the linear and cubic terms) to better capture the form of the flow profile. This is because as g becomes large we may generate viscous heating in the fluid and induce variations in the fluid viscosity, which will appear as higher-order nonlinearities in the spatial dependence of velocity[28]. We observe remarkable agreement between this fit and the data points which lie outside the fitting domain. The average relative errors between the fit and the data outside the domain is 6.4% (for the c_{fw} data) and 7.8% (for the g data).

The calculated slip lengths as a function of c_{fw} and g can be seen in Figs. 4 and 5. It is clear that a reduced wall-fluid interaction results in a larger slip length. We also observe that as c_{fw} is increased the slip length crosses from the negative region (outside the wall position that we defined in Section IV A) to the positive region (inside the walls) at $c_{\mathrm{fw}} \simeq 0.85$. This behaviour is intuitive as we expect that, as c_{fw} increases, the first fluid layer begins to immobilize and behave almost as if it were another layer of wall particles. As the acceleration is varied we also observe an increase of slip with g as well as the crossover from positive slip to negative slip (which has been observed in similar MD simulations by others[29]).

Note that the first fluid layer in Fig. 2 is approximately $\frac{1}{2}\sigma$ from the wall position and also that the slip lengths in Figs. 4 and 5 go to approximately this value for $c_{\mathrm{fw}} = 1$ and as $g \to 0$. If the first liquid layer is immobile, which should be the case under conditions of pure LJ interaction and low acceleration, then it is intuitive that the slip length should correspond to the position of this fixed particle layer. The value of c_{fw} also affects the layering of the

particle distribution function near the wall. We can see in the inset of Fig. 4 that the first layer of fluid is further and further from the wall particles as $c_{\rm fw}$ increases. From Eq. 2 we can derive the position of the minimum in the potential, and thus the point of zero force, where a pair of equilibrium particles would prefer to sit. This is given by $r_{\rm min} = (2/c_{\rm fw})^{\frac{1}{6}}\,\sigma$. However, this fluid layer will still feel pressure from fluid inside the channel. Nevertheless, the observed increase in $r_{\rm min}$ with decreasing $c_{\rm fw}$ is indeed expected but the fluid pressure causes this shift to be less than 1% whereas the predicted shift in $r_{\rm min}$ should be 12%. Note that as the attractive interaction is reduced, the first fluid layer moves away from the wall but its probability distribution broadens. This reflects the fact that these particle layers are increasingly acting like bulk fluid, as opposed to tightly packed layers.

V. RESULTS II: THE CHANNEL PLUS CAVITY

A. Angular Momentum in the Cavity

Surprisingly, it takes very few MD timesteps to accelerate the cavity fluid into equilibrium rotational motion. However, to err on the conservative side and ensure the data represents equilibrium, we neglect data for a significant early portion of the simulation. To quantify the level of "spin" in a given simulation we have calculated the total angular momentum of the cavity particles (those particles whose positions lie above the position of the upper wall, effectively inside the cavity) with respect to the point of zero rotation. This point, $\boldsymbol{r_0}$, is determined from velocity fields and streamlines such as those shown in Fig. 6 and the total angular momentum per particle (i.e., mass-averaged since all particles have the same mass, $m = 1$) is calculated as a sum over each using the basic relation $\bar{J} = \left|\left|\sum_{i=1}^{N} \boldsymbol{r_i} \times \boldsymbol{p_i}\right|\right| /N$, where $\boldsymbol{r_i}$ is the position of the $i^{\rm th}$ particle from $\boldsymbol{r_0}$ and $\boldsymbol{p_i}$ is its momentum. For better statistics, we have used a time-averaged angular momentum per particle: $\langle \bar{J} \rangle$.

The angular momentum is calculated from several simulations with varying interaction strengths and accelerations. We observe that as g is increased (with a constant $c_{\rm fw} = 1$) there is a corresponding increase in $\langle \bar{J} \rangle$ since the slip at the wall becomes significant (Fig. 7). In order to explore how $c_{\rm fw}$ influences the rotation of the cavity fluid, we use two different schemes. In the first scheme (hereafter referred to as scheme A), only the particles along the upper channel wall have a reduced interaction strength ($0.5 \leq c_{\rm fw} < 1$). In the second

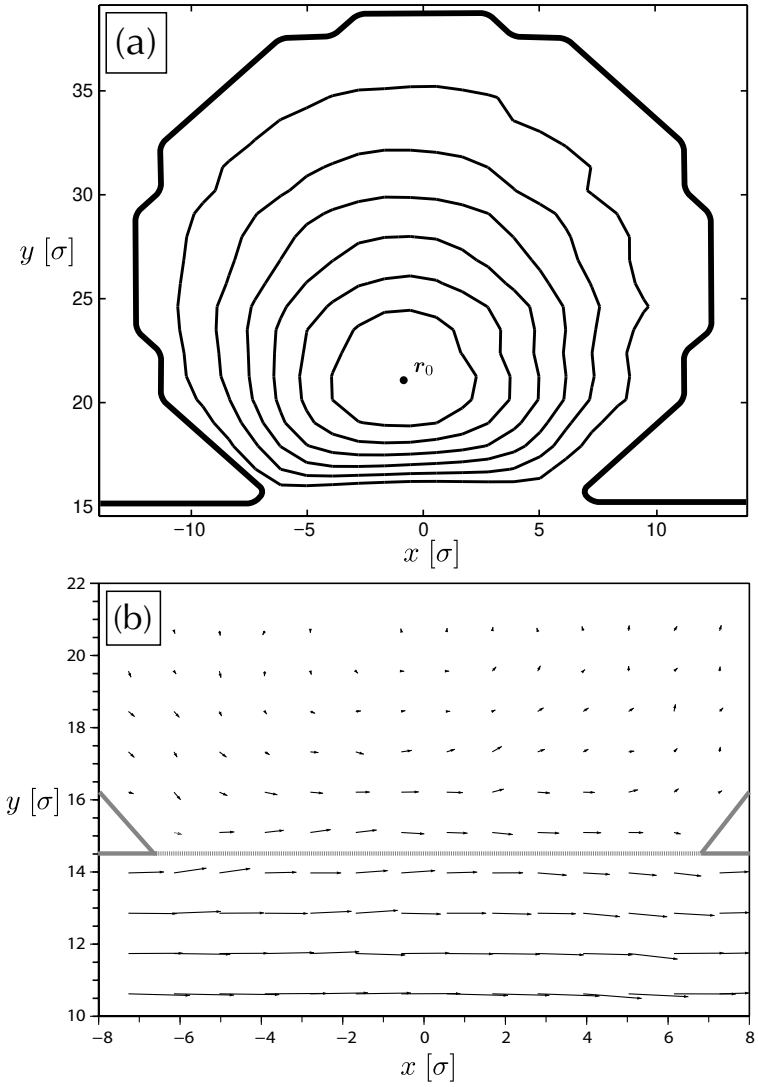

FIG. 6: Time-averaged velocity field and streamlines computed from the velocity field for $c_{\mathrm{fw}} = 0.5$ and $g = 0.025\ \sigma/\tau^2$ using scheme B. The velocity field is calculated by averaging the steady-state particle velocities in two-dimensional bins. (a) shows the rotation of the fluid in the cavity. Closed streamlines, of course, represent circulation of fluid particles. The thick black line represents the approximate location of boundary between the fluid and the cavity walls. (b) shows the continuity of velocity across the coupling region. The solid gray lines denote the approximate location of the fixed wall and the dotted gray line shows the coupling region between the cavity and the channel.

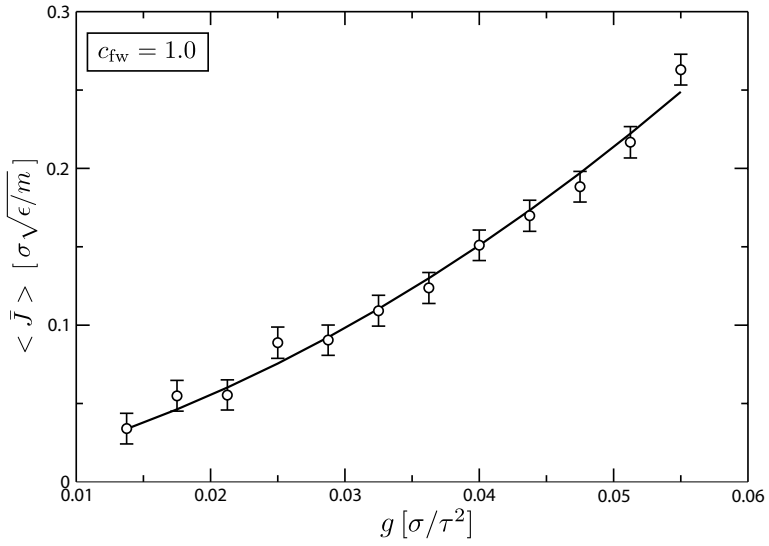

FIG. 7: Average angular momentum per particle in the cavity for various accelerations with no modification of wall-fluid interactions (i.e., $c_{\rm fw} = 1$). As expected, the average angular momentum of the fluid inside the cavity increases as a function of g. The empirical fit $\langle \bar{J} \rangle = ag(1 + g/g_0)$ is shown with parameters $a = 1.77 \pm 0.13\sigma\ \sqrt{\epsilon/m}$ and $g_0 = 0.0353 \pm 0.0026\ \sigma/\tau^2$. The latter value is thus an estimate of the critical acceleration which indicates the onset of nonlinearity.

scheme (scheme B), both the channel wall and the cavity wall particles have been modified. In scheme A, the effect should be that observed above: the slip length and thus the fluid velocity increases at the wall. This will result in a larger force coupled to the cavity fluid and thus we would expect an increase in angular momentum with increasing slip length (i.e., a decrease in $c_{\rm fw}$). Scheme B will compound the previous effect with a simultaneous reduction in friction between the fluid and the cavity wall. In both schemes we have used the same values of $c_{\rm fw}$ as those used in Section IV D and the results can be seen in Fig. 8 (for a constant $g = 0.025\ \sigma/\tau^2$). We see a clear increase in angular momentum with decreasing surface tension.

We would expect the system to behave simply (perhaps linearly) in well understood regimes where we use parameter values commonly seen in the literature (i.e., pure Lennard-Jones with $c_{\rm fw} = 1$, low acceleration g). As we move away from this regime we should start to observe the onset of nonlinearity at some critical value of these parameters. Velocity profiles for high g (not shown here) take the form of quadratic Poiseuille profiles superimposed

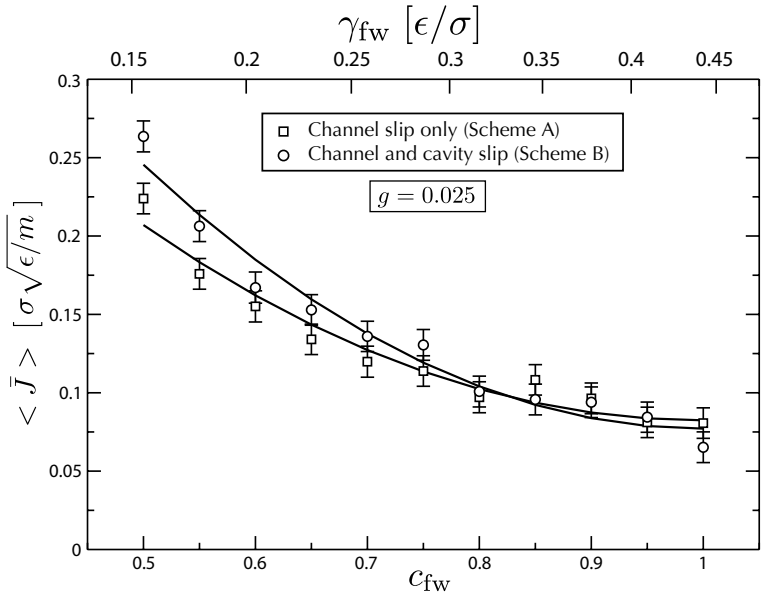

FIG. 8: Average angular momentum per particle in the cavity for various wall-fluid interaction strengths (acceleration is constant at $g = 0.025\,\sigma/\tau^2$). Results are shown from simulations where only the channel walls have modified interaction and those where both the channel and cavity walls are modified. The average angular momentum of the fluid inside the cavity increases when $c_{\rm fw}$ increases. We also observe that the two schemes differ from each other as $c_{\rm fw}$ decreases. The empirical fit $\langle \bar{J} \rangle = J_0(1 + c^{*2}/c_0^{*2})$ where $c^* = 1 - c_{\rm fw}$ is shown. The parameters are $J_0 = 0.0824 \pm 0.0055\,\sigma\sqrt{\epsilon/m}$ and $c_{\rm fw,0} = 0.593 \pm 0.040$ for scheme A and $J_0 = 0.0771 \pm 0.0065\,\sigma\sqrt{\epsilon/m}$ and $c_{\rm fw,0} = 0.662 \pm 0.051$ for scheme B.

with a small amplitude nonlinearity of order y^4. This higher order nonlinearity increases in amplitude with g. Furthermore, the profiles become increasingly offset from zero due to the slip at both walls generated by the high acceleration. We estimate the critical values by performing the following empirical fits: $\langle \bar{J} \rangle = ag(1 + g/g_0)$ for varying g and $\langle \bar{J} \rangle = J_0(1 + c^{*2}/c_0^*)$ for varying $c_{\rm fw}$, where $c^* = 1 - c_{\rm fw}$. We have chosen to fit c^*, as defined, rather than $c_{\rm fw}$ directly since the system should exhibit "normal" properties about the pure LJ regime which is $c_{\rm fw} = 1$ and thus $c^* = 0$ (the origin). The results are shown in Figs. 7 and 8 and yield the critical values of $g_0 = 0.0353 \pm 0.0001\,\sigma/\tau^2$, $c_{\rm fw,0} = 0.593 \pm 0.001$ for scheme A and $c_{\rm fw,0} = 0.662 \pm 0.001$ for scheme B. The critical value of g_0 matches well with the data seen in Section IV D as it represents the point at which the slip length begins to level off to $\delta \sim \sigma/2$ in Fig. 5. The critical values of $c_{\rm fw}$ are also relevant as they indicate where the slip

length becomes highly nonlinear in Fig. 4.

We would expect that since scheme A has a weaker wall-fluid interaction overall, it will be less effective than scheme B at spinning the cavity fluid. It is not clear that we observe this as a generality across all parameter values. For low surface tensions, where the cavity is being driven hard, scheme B is clearly more effective than scheme A but not by much (at most there is a 19% increase, at $c_{\mathrm{fw}} = 0.5$). However, for higher values of surface tension where the cavity is being driven by a weaker flow (i.e., the slip at the wall is smaller) the difference between the two schemes is no longer systematic and is on the order of the noise in the data.

We can visualize the fluid motion in the cavity by looking at the two-dimensional velocity field. This can be seen in Fig. 6 for a simulation with $c_{\mathrm{fw}} = 0.5$ using scheme B. Figure 6a demonstrates the rotational motion of the fluid in the cavity with streamlines, found by integrating the velocity field. It should be noted that the stagnation point of the flow is not in the centre of the circular cavity and is in fact closer to the coupling region: presumably, this is dependent on the fluid properties, such as viscosity, the cavity size and offset although we are not exploring this in the current study. Also presented in Fig. 6b is a higher resolution velocity field focused on the coupling region of the channel-cavity system illustrating the continuity of the velocity field across the interface and clear coupling between the cavity and channel fluids.

B. Velocity Dependence of Angular Momentum

In order to predict how the angular momentum of the cavity fluid should depend on the properties of the system we performed calculations based on the predictions of macroscopic hydrodynamics. The 2D incompressible Navier-Stokes equation for a Newtonian fluid[15] can be expressed in terms of vorticity ω and the streamfunction ψ as

$$\frac{\partial \omega}{\partial t} + \boldsymbol{u} \cdot \nabla \omega = \frac{\eta}{\rho_0} \nabla^2 \omega, \tag{8}$$

$$-\nabla^2 \psi = \omega, \tag{9}$$

where $\boldsymbol{u} = u\hat{\mathrm{x}} + v\hat{\mathrm{y}}$, $\partial\psi/\partial y = u$, $\partial\psi/\partial x = -v$ and $\omega = ||\nabla \times \boldsymbol{u}||$. To model our system we use a circular boundary with a piece cut out by intersecting a horizontal straight line near the lower edge. The boundary conditions are zero velocity around the circular edge and a

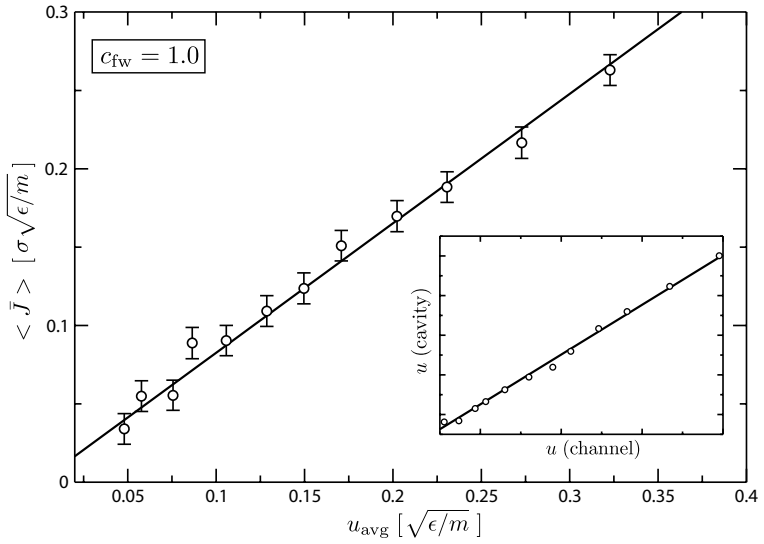

FIG. 9: The dependence of average angular momentum $\langle \bar{J} \rangle$ from the MD simulations on average forcing velocity ($u_{\rm avg} = (u_{\rm chan} + u_{\rm cav})/2$). The wall-fluid interaction is kept constant with $c_{\rm fw} = 1.0$. The fit is linear with zero intercept: $\langle \bar{J} \rangle = (0.83 \pm 0.01) u_{\rm avg}$. The inset shows the linear relationship between $u_{\rm cav}$ and $u_{\rm chan}$ with a slope of 0.63 ± 0.01.

constant tangential velocity $\boldsymbol{u} = V\hat{\mathrm{x}}$ at the straight edge. This latter condition emulates the external forcing at the coupling region we see in our MD simulations (at equilibrium). The total angular momentum is calculated, as before, by finding the stagnation point $\boldsymbol{r_0}$ and integrating $(\boldsymbol{r} - \boldsymbol{r_0}) \times \rho_0 \boldsymbol{u}$ over the area of the cavity.

Equations 8 and 9 are solved using finite difference (FD) methods, with parameters chosen so that Re $= O(1)$. The FD calculations are formulated using a forward in time and centred in space differencing scheme for the vorticity equation (Eq. 8) and an iterative, successive over-relaxation scheme with centred differences for the streamfunction equation (Eq. 9). Stepsizes in both spatial directions are equal ($\Delta x = \Delta y = \Delta$) and the timestep is chosen such that is satisfies the CFL condition for stability: $\Delta t \leq \Delta^2 \rho_0 / 4\eta$. We will not explicitly show the results of these calculations as they simply suggest that the average angular momentum $\langle \bar{J} \rangle$ should increase linearly with V such that $\langle \bar{J} \rangle = \alpha V$ (where α is some proportionality constant).

We will use this prediction to help explain our MD results and so must first determine how to relate the parameters from MD to those in the FD calculations. Clearly, the mass

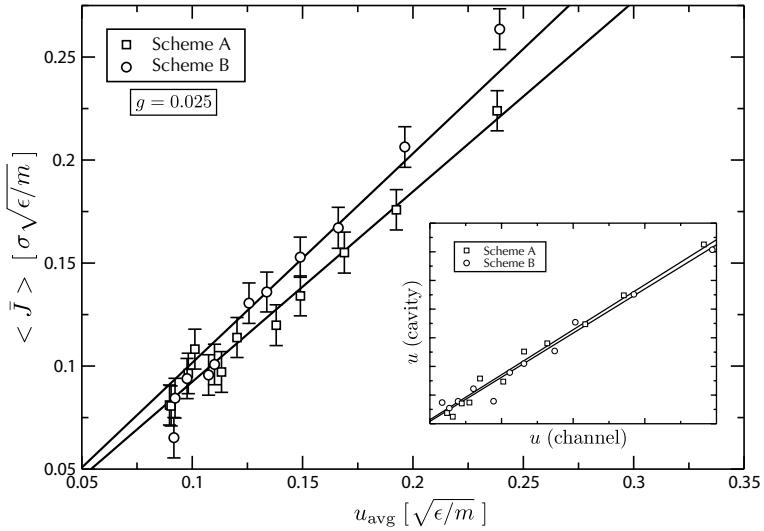

FIG. 10: The dependence of average angular momentum $\langle \bar{J} \rangle$ from the MD simulations on average forcing velocity ($u_{\rm avg} = (u_{\rm chan} + u_{\rm cav})/2$). The acceleration is constant at $g = 0.025\ \sigma/\tau^2$ and the wall fluid interaction ranges from $c_{\rm fw} = 0.5$ to $c_{\rm fw} = 1.0$. The fit is linear with zero intercept: $\langle \bar{J} \rangle = \alpha u_{\rm avg}$ with proportionality constants $\alpha_{\rm A} = 0.92 \pm 0.01$ and $\alpha_{\rm B} = 1.02 \pm 0.01$. The inset shows the linear relationship between $u_{\rm cav}$ and $u_{\rm chan}$. The slopes are 0.63 ± 0.01 for scheme A and 0.62 ± 0.01 for scheme B.

averaged angular momentum from the FD calculations is equivalent to the average angular momentum per MD particle: $\langle \bar{J} \rangle$. We will make the correspondence between the forcing speed V and the average speed of fluid at the wall in the vicinity of the cavity in the MD simulations. This velocity, $u_{\rm avg}$, is defined as the average over the region along x adjacent to the coupling interface and over two layers of fluid particles (both inside and outside the cavity, $u_{\rm cav}$ and $u_{\rm chan}$ respectively). From the FD predictions, we should observe a linear relationship between the velocity of two layers of fluid particles we average over and thus the average should not disrupt the linear relationship between angular momentum and velocity.

We present the average angular momentum plotted versus the average forcing velocity about the coupling region in Figs. 9 and 10 (for varying g and $c_{\rm fw}$, respectively). Also, the linear relationship between the two velocities is shown in the insets. For the angular momentum, each data set is fit with the expected relationship $\langle \bar{J} \rangle = \alpha u_{\rm avg}$, with good agreement especially using scheme A. However, it is not clear whether the results for scheme B should be linear in any case. The predictions from macroscopic hydrodynamics were for

a system with zero velocity at the cavity walls but, as we observed in Section IV D, when the wall-fluid interaction is modified (as it is in scheme B) there exists a non-zero slip and thus the zero velocity boundary condition should not hold.

C. Efficiency of "Spin" Generation

To demonstrate that we are in a similar regime as that existing in previous experiments[2–4] we will formulate a nondimensional parameter to characterize the system based on the cavity spin, dimension and channel flow. Let us define the dimensionless Spin number, S, as the ratio between the product GR, where G is the radial acceleration in the cavity and R is its radius, and the square of the average fluid velocity in the channel $\bar{u}$:

$$S \equiv \frac{GR}{\bar{u}^2}. \tag{10}$$

The values observed experimentally are $G = 1.4 \times 10^7$ m/s^2, $R \simeq 50$ μm and $\bar{u} = 45$ m/s^2 which yield a dimensionless Spin number of $S = 0.345$. From our simulation data for $c_{\text{fw}} = 0.5$ and $g = 0.025\ \sigma/\tau^2$ we have $G = 0.00559\ \sigma/\tau^2$ (the maximum radial acceleration, which is observed just inside the coupling region), $R = 12.3\ \sigma$ and $\bar{u} = 0.819\ \sigma/\tau$. Using these values we calculate the Spin number to be $S = 0.103$ which is of the same order of magnitude as that observed experimentally.

In Figs. 9 and 10 we observe approximately the same range of angular momentum in the cavity over the same range of forcing speeds for all of the various schemes we have employed to spin the cavity fluid. In fact, our results indicate that by keeping g at a reasonable value and modifying the wall-fluid interaction we can achieve cavity spin comparable to that achieved by pushing the fluid harder. As an example, let us take simulations from all three cases with approximately the same flow rate in the channel: $\bar{u} \simeq 0.728 \pm 0.005\ \sigma/\tau$. If we keep the wall-fluid interaction as pure wetting ($c_{\text{fw}} = 1$) then we need an acceleration of $g \simeq 0.029\ \sigma/\tau^2$ to achieve this flow rate and it results in an average angular momentum in the cavity of $\langle \bar{J} \rangle = 0.0904\ \sigma\sqrt{\epsilon/m}$. For the cases where the wall fluid interaction is modified we use an acceleration of $g = 0.025\ \sigma/\tau^2$ and to achieve the above flow rate we require $c_{\text{fw}} = 0.6$ which results in average angular momenta of $\langle \bar{J} \rangle = 0.1573\ \sigma\sqrt{\epsilon/m}$ for scheme A and $\langle \bar{J} \rangle = 0.1679\ \sigma\sqrt{\epsilon/m}$ for scheme B. This is effectively an increase of 71% in scheme A and 82% in scheme B for a 54% decrease in surface tension.

VI. CONCLUSIONS

Shelby *et al.* have performed exciting experimental research and we have reproduced and expanded upon their basic idea. Using Molecular Dynamics, we have simulated spin generation in a coupled cavity-channel system which lies in the same physical regime as that seen in experiments. From these simulations we observed the finite structure of the fluid and have shown that its hydrodynamic properties are laminar. We were able to make the connection between surface tension of the wall-fluid interface and the hydrophobicity of the wall by analysing the fluid slip along the wall. In particular, we can simulate systems with hydrophobicity without making assumptions about boundary conditions. These principles can be applied to a coupled cavity-channel system to control the angular momentum in the cavity. We were able to increase the level of spin in the cavity by over 80%. Predictions from macroscopic hydrodynamics were succesfully reproduced, showing that even when the finite structure of the fluid is observable these predictions can still hold. Molecular Dynamics has shown itself to be useful for exploring systems that would be difficult using traditional means (i.e., modelling hydrophobicity with hydrodynamics).

We are exploring how the spin depends on the size of the coupling region between the cavity and the channel. It is clear that there must be an optimal coupling length if we consider the extreme cases: if the length is very large (i.e., the cavity offset is less than zero), the channel fluid will simply stream into the cavity and back out again, producing no spin and if the length is very small, the coupling between the channel and the cavity will be weak and therefore spin will be very low. Between the two extreme cases there must be an optimal length for inducing spin with the least amount of input energy. Our simulations use an intermediate sized coupling region and so we believe the results to be representative of the physics near the optimal system. This study could be extended to explore the system as the width of the channel W or the cavity radius R are reduced to the nanoscale. (In other words, how do the physics scale as the system dimensions approach the nanometre regime.) Molecular Dynamics allows us to explore layering of the fluid near walls which would be dominant on nanoscopic length scales. Also, there must be some exchange of mass between the channel and the cavity and so it would be interesting to explore this and how it might impact the use of the cavity as a centrifugation cell, particularly the centrifugation of polymeric substances which can be easily implemented in our Molecular Dynamics model.

VII. ACKNOWLEDGEMENTS

G. W. S. would like to acknowledge the financial support of a Natural Science and Engineering Research Council (NSERC) Discovery grant. E. C. J. O. would like to acknowledge the financial support of the Sun Microsystems of Canada Scholarship, the Nunatsiavut Government PSSSP and the University of Ottawa Admissions Scholarship. Furthermore, E. C. J. O. would like to thank F. Tessier, M. Kenward, S. Casault, M. Bertrand and L. Taylor for discussions, assistance and support in the preparation of this work.

---

* Electronic address: `eric.oliver@dal.ca`

† Electronic address: `gslater@uottawa.ca`

[1] T. M. Squires and S. R. Quake. Microfluidics: Fluid physics at the nanoliter scale. *Rev. Mod. Phys.*, 77:977–1026, 2005.

[2] J. P. Shelby, D. S. W. Lim, J. S. Kuo, and D. T. Chiu. High radial acceleration in microvortices. *Nature*, 425:38, 2003.

[3] J. P. Shelby and D. T. Chiu. Controlled rotation of biological micro- and nano-particles in microvortices. *Lab Chip*, 4:168–170, 2004.

[4] J. P. Shelby, S. A. Mutch, and D. T. Chiu. Direct manipulation and observation of the rotational motion of single optically trapped microparticles and biological cells in microvortices. *Anal. Chem.*, 76:2492–2497, 2004.

[5] D. C. Rapaport and E. Clementi. Eddy Formation in Obstructed Fluid Flow: A Molecular-Dynamics Study. *Phys. Rev. Lett.*, 57:695–698, 1986.

[6] D. C. Rapaport. Microscale hydrodynamics: Discrete-particle simulation of evolving flow patterns. *Phys. Rev. A*, 36:3288–3299, 1987.

[7] D. C. Rapaport. Molecular-Dynamics Study of Rayleigh-Bénard Convection. *Phys. Rev. Lett.*, 60:2480–2483, 1988.

[8] M. Mareschal, M. Malek Mansour, A. Puhl, and E. Kestemont. Molecular Dynamics versus Hydrodynamics in a Two-Dimensional Rayleigh-Bénard System. *Phys. Rev. Lett.*, 61:2550–2553, 1988.

[9] T. Ishiwata, T. Murakami, S. Yukawa, and N. Ito. Particle Dynamics Simulations of the Navier-

Stokes Flow with Hard Disks. *Int. J. Mod. Phys. C*, 15:1413–1424, 2004.

[10] G. P. Morriss. The breakdown of Navier-Stokes hydrodynamics in small periodic systems. *Mol. Phys.*, 100(14):2377–2386, 2002.

[11] D. M. Heyes, G. P. Morriss, and D. J. Evans. Nonequilibrium molecular dynamics study of shear flow in soft disks. *J. Chem. Phys.*, 83:4760–4766, 2006.

[12] B. Smit and D. Frenkel. Vapor-liquid equilibria of the two-dimensional lennard-jones fluid(s). *J. Chem. Phys.*, 94:5663–5668, 1991.

[13] A. K. Prasad and J. R. Koseff. Reynolds number and end-wall effects on a lid-driven cavity flow. *Phys. Fluids A-Fluid*, 1:208, 1989.

[14] J. R. Koseff, A. K. Prasad, C. Perng, and R. L. Street. Complex cavities: Are two dimensions sufficient for computation? *Phys. Fluids A-Fluid*, 2:619, 1990.

[15] P. K. Kundu and I. M. Cohen. *Fluid Mechanics*. Academic Press, San Diego, CA, second edition, 2002.

[16] J. Koplik and J. R. Banavar. Continuum deductions from molecular hydrodynamics. *Annu. Rev. Fluid Mech.*, 27:257–292, 1995.

[17] D. C. Rapaport. *The Art of Molecular Dynamics Simulation*. Cambridge University Press, Cambridge, 1995.

[18] T. Soddeman, B. Dünweg, and K. Kremer. Dissipative particle dynamics: A useful thermostat for equilibrium and nonequilibrium molecular dynamics simulations. *Phys. Rev. E*, 68:046702–1–8, 2003.

[19] E. A. J. F. Peters. Elimination of time step effects in dpd. *Europhys. Lett.*, 66:311–317, 2004.

[20] F. Tessier and G. W. Slater. Modulation of electroosmotic flow strength with end-grafted polymer chains. *Macromolecules*, 39:1250–1260, 2006.

[21] J. S. Rowlinson and B. Widom. *Molecular Theory of Capillarity*. Oxford University Press, Oxford, 1987.

[22] J.-L. Barrat and L. Bocquet. Large slip effect at a nonwetting fluid-solid interface. *Phys. Rev. Lett.*, 82:4671, 1999.

[23] J. Koplik and J. R. Banavar. No-slip condition for a mixture of two liquids. *Phys. Rev. Lett.*, 80:5125–5128, 1998.

[24] J. Koplik and J. R. Banavar. Molecular Simulations of Dewetting. *Phys. Rev. Lett.*, 84:4401–4404, 2000.

[25] U. Heinbuch and J. Fischer. Liquid flow in pores: Slip, no-slip, or multilayer sticking. *Phys. Rev. A*, 40(2):1144–1146, 1989.

[26] N. V. Priezjev, A. A. Darhuber, and S. M. Troian. Slip behavior in liquid films on surfaces of patterned wettability: Comparison between continuum and molecular dynamics simulations. *Phys. Rev. E*, 71(4):41608, 2005.

[27] M. J. P. Nijmeijer, C. Bruin, A. F. Bakker, and J. M. J. van Leeuwen. Wetting and drying of an inert wall by a fluid in a molecular-dynamics simulation. *Phys. Rev. A*, 42(10):6052–6059, 1990.

[28] K. P. Travis. Poiseuille flow of Lennard-Jones fluids in narrow slit pores. *J. Chem. Phys.*, 112:1984, 2000.

[29] Y. L. Gratton and G. W. Slater. Molecular dynamics study of tethered polymers in shear flow. *Eur. Phys. J. E*, 17:455–465, 2005.